# Numerical Study of Penetrative and "Solid Lid" Nonpenetrative Convective Boundary Layers

ZBIGNIEW SORBJAN

*School of Meteorology, University of Oklahoma, Norman, Oklahoma*

(Manuscript received 11 April 1995, in final form 22 June 1995)

ABSTRACT

A large eddy simulation model was used to generate and compare statistics of turbulence during nonpenetrative and penetrative dry convection. In penetrative convection dimensionless vertical velocities in updrafts were found to have almost the same values as in the nonpenetrative case. The countergradient transport of heat and moisture was found to be present during nonpenetrative convection at $z/z_i > 0.6$. For penetrative convection the countergradient transport of heat occurred only in a layer $0.5 < z/z_i < 0.75$, while the countergradient transport of humidity was not present. During nonpenetrative convection, temperature and humidity were perfectly correlated. In penetrative convection the correlation coefficient was found to be less than unity, varying from about 0.9 near the surface to about $-0.7$ at the top of the mixed layer.

## 1. Introduction

Convection occurs in a broad range of forms and scales. It can be observed in a container of heated liquid, as well as in the atmosphere or in a lake. Convection takes the form of hexagonal cells or horizontal rolls sometimes marked by a presence of clouds in the atmosphere (e.g., Agee 1987) or it is exhibited as foam patterns on lake surfaces. During the last three decades, laboratory and numerical research have led to the accumulation of qualitative and quantitative knowledge of atmospheric convection.

Basic aspects of convection were explored with the convection tank (e.g., Deardorff et al. 1969; Willis and Deardorff 1974; Deardorff et al. 1980; Adrian et al. 1986; Kumar and Adrian 1986). An important portion of the present understanding of the convectively mixed layer was achieved through numerical simulations, first through large eddy simulations (LESs) and later through direct numerical simulations (DNSs). The advantage of such simulations is based on the fact that both LESs and DNSs use equations that are derivable from the exact set and, hence, remain faithful to the essential physics of the flow (e.g., Nieuwstadt 1990; Wyngaard 1992; Mason 1994). The first numerical large eddy simulations were performed by Deardorff (1972, 1973a,b, 1974). Large eddy simulations of atmospheric convection were later investigated by for example, Schemm and Lipps (1976), Sommeria (1976), Moeng (1984), Nieuwstadt and Brost (1984), Sykes and Henn (1988), Schmidt and Schumann (1989), and Mason (1989). Direct simulation of the atmospheric boundary layer were performed by, for example, Krettenauer and Schumann (1992) and Coleman et al. (1990). LES and DNS models proved to be attractive sources of turbulent data, especially because of known difficulties with assembling suitable databases on atmospheric turbulence.

One of the basic features of atmospheric boundary layer convection is the exchange of mass, momentum, and heat between the top of the mixed layer and the stably stratified layer above. The exchange is triggered by thermals penetrating the stable layer and forcing entrainment of warmer air into the mixed layer (Deardorff et al. 1980). Effects of entrainment are important to the structure of the mixed layer and have been studied experimentally (e.g., Caughey and Palmer 1979; Young 1988) and also numerically (e.g., Deardorff 1974). Based on these studies, numerous parameterization schemes been presented (e.g., Lilly 1968; Zeman and Tennekes 1977; Mahrt 1979; Boers 1989).

An interesting aspect of convection was reported by Adrian et al. (1986) during their nonpenetrative (without entrainment) convection experiments in a tank. The tank, 1.45 m × 1.5 m × 0.2 m in size, was heated from below by electrical mats and had an insulated solid lid at the top. The results obtained showed an intriguing resemblance of various turbulence statistics in the lower portion of the nonpenetrative mixed layer and in the penetrative atmospheric boundary layer. Nonpenetrative convection in a tank was successfully simulated by Krettenauer and Schumann (1992) by using LES

*Corresponding author address:* Dr. Zbigniew Sorbjan, School of Meteorology, Energy Center, Room 1518, University of Oklahoma, 100 West Boyd St., Norman, OK 73019-0470.
E-mail: zsorbjan@tornado.uoknor.edu

and DNS models. Krettenauer and Schumann demonstrated that numerical results can be taken to be as reliable as laboratory measurements.

The goal of this study is to also simulate numerically the nonpenetrative dry boundary layer using an LES model. Nevertheless, the focus of this paper is different. We intend to compare the obtained results for nonpenetrative convection with the numerical simulation of the penetrative convection in the atmosphere. With such a comparison, we aim to study the fundamental factor that distinguishes both cases, that is, the entrainment on the top of the convective atmospheric boundary layer.

## 2. Model description

### a. Basic equations

The LES model applied in this study is based on a system of the differential equations consisting of conservation laws for momentum, mass, and the first law of thermodynamics (e.g., Deardorff 1973a,b; Lilly 1987; Nieuwstadt 1990):

$$\frac{\partial \overline{u_i}}{\partial t} + \frac{\partial \overline{u_i u_j}}{\partial x_j} = -\frac{\partial \pi}{\partial x_j} + \beta(\bar{\theta} - \theta_0)\delta_{ij} - 2\epsilon_{ijk}\Omega_j \bar{u}_k - \frac{\partial \tau_{ij}}{\partial x_j}$$

$$\frac{\partial \bar{\theta}}{\partial t} + \frac{\partial \overline{u_j}\bar{\theta}}{\partial x_j} = -\frac{\partial H_j}{\partial x_j}$$

$$\frac{\partial \bar{q}}{\partial t} + \frac{\partial \overline{u_j}\bar{q}}{\partial x_j} = -\frac{\partial Q_j}{\partial x_j}$$

$$\frac{\partial \overline{u_j}}{\partial x_j} = 0, \qquad (1)$$

where $x_j$ are the Cartesian coordinates ($i = 1, 2, 3$), $x_3$ is parallel to gravity acceleration, $\overline{u_i}$ are the components of the velocity vector, $\bar{\theta}$ and $\bar{q}$ are the perturbations of the virtual potential temperature and specific humidity with respect to the reference state values that are chosen to be constant with height, $\pi = \bar{P} + \frac{2}{3}E$ is the air pressure perturbation modified by adding a term proportional to the subgrid turbulent kinetic energy $E = \frac{1}{2}(\overline{u_k u_k} - \overline{u_k}\,\overline{u_k})$, $\bar{P} = (\bar{p} - p_0)/\rho_0$ is the pressure perturbation term, $\tau_{ij} = (\overline{u_i u_j} - \overline{u_i}\,\overline{u_j}) - \frac{2}{3}E\delta_{ij}$ is the stress tensor (note that $\tau_{kk} = 0$), $H_j = (\overline{u_j\theta} - \overline{u_j}\bar{\theta})$ is the subgrid turbulent temperature flux, $Q_j = (\overline{u_j q} - \overline{u_j}\bar{q})$ is the subgrid turbulent humidity flux, $\beta = g/\theta_0$ is the buoyancy parameter, $\Omega_j$ is the component of the earth's angular velocity, $\delta_{ij}$ is Kronecker's delta, and $\epsilon_{ijk}$ is the unity tensor; $\theta_0$, $p_0$ are the reference state potential temperature and pressure. The overbar indicates a running grid volume average:

$$\bar{f}(x, y, z) = \frac{1}{\Delta x \Delta y \Delta z}\int_{x-\Delta x}^{x+\Delta x}\int_{y-\Delta y}^{y+\Delta y}\int_{z-\Delta z}^{z+\Delta z} \times f(X, Y, Z)\,dX\,dY\,dZ, \qquad (2)$$

where $\Delta x$, $\Delta y$, $\Delta z$ are the grid increments. It can be proved that $\bar{\bar{f}} \neq \bar{f}$ and that the averaging operator commutes: $\partial\bar{f}/\partial x_k = \overline{\partial f/\partial x_k}$. The use of potential temperature in nondivergent system is approximate, although admittedly common (Lilly 1995).

### b. Subgrid model

The set (1) of grid volume-averaged equations constitutes a system of six differential equations with six unknown quantities: $\overline{u_1}$, $\overline{u_2}$, $\overline{u_3}$, $\bar{\theta}$, $\bar{q}$, and $\pi$. The system (1) also contains three "subgrid" terms $\tau_{ij}$, $H_j$, $Q_j$, which have to be related to the grid volume-averaged variables. The subgrid fluxes are parametrized as follows (e.g., Deardorff 1973a,b):

$$\tau_{ij} = -k_m\left(\frac{\partial \overline{u_i}}{\partial x_j} + \frac{\partial \overline{u_j}}{\partial x_i}\right)$$

$$H_j = -k_h\frac{\partial \bar{\theta}}{\partial x_j}$$

$$Q_j = -k_q\frac{\partial \bar{q}}{\partial x_j}, \qquad (3)$$

where $k_m$ is the eddy viscosity, and $k_h$ and $k_q$ are the eddy diffusivities. The eddy viscosity and diffusivity coefficients are assumed to be functions of the subgrid turbulent kinetic energy $E$, mixing length $\lambda$, and the Prandtl number Pr:

$$k_m = c_m\lambda E^{1/2}$$

$$k_h = k_q = k_m/\mathrm{Pr}. \qquad (4)$$

The subgrid turbulent kinetic energy $E$ satisfies the following prognostic equation, which can be derived based on the set (1) (e.g., Lilly 1987):

$$\frac{\partial E}{\partial t} + \frac{\partial \overline{u_j}E}{\partial x_j} = -\tau_{ij}\frac{\partial \overline{u_i}}{\partial x_j} + \beta H_3 - \frac{\partial}{\partial x_j}(T_j + P_j) - \epsilon, \qquad (5)$$

where $\epsilon$ is the viscous dissipation rate, $T_j$ is the turbulent transport term, and $P_j = (\overline{\pi u_j} - \bar{\pi}\,\overline{u_j})$ is the pressure term. The first and the last terms on the right-hand side are expected to be dominant during free convection.

The turbulent transport, pressure, and dissipation terms in (5) can be parametrized in the following way (e.g., Deardorff 1973a,b):

$$P_j + T_j = -c_e k_m\frac{\partial E}{\partial x_j} \qquad (6)$$

$$\epsilon = c_\epsilon\frac{E^{3/2}}{\lambda}, \qquad (7)$$

where $c_e$ and $c_\epsilon$ are constants and $\lambda$ is the mixed length. The mixing length was defined as (Schumann 1991a)

$$\lambda = \min(\Delta, c_L z), \qquad (8)$$

where the parameter $\Delta = (\Delta x + \Delta y + \Delta z)/3$ must fall within the inertial subrange. The following numerical values of constants were adopted: $c_\epsilon = 0.845$, $c_e = 2.0$, $c_m = 0.0856$, $c_h = 0.204$, and $c_L = 0.845$ (Schumann 1991a).

Following Schumann (1991a), it was assumed that $\mathrm{Pr} = k_m/k_h = c_m/c_h$. In stably stratified parts of the flow the vertical subgrid heat and scalar fluxes were modified by assuming that $\mathrm{Pr} = (c_m/c_h)[1 + 0.3\Delta^2(N^2/E)]$, where $N = (\beta\partial\bar{\theta}/dz)^{0.5}$ is the Brunt–Väisälä frequency. The modification reduces the values of eddy diffusivities: $k_h = k_m/\mathrm{Pr} = c_h\lambda E^{3/2}/(E + 0.3\Delta^2N^2)$. The reduction can be explained by the fact that in stable conditions all vertical motions including diffusion are opposed by buoyancy. For very stable stratification, $\Delta^2N^2 \gg E$, and $k_h \to c_hE^{3/2}/(0.3\Delta N^2)$, which agrees with results obtained previously by Lilly et al. (1974) and Weinstock (1978).

The constants $c_m$ and $c_\epsilon$ can be related to the Smagorinsky constant $c_s$ as $c_s = c_m^{3/4}/c_\epsilon^{1/4}$ (e.g., Sullivan et al. 1994). For the constants listed above one can obtain $c_s = 0.163$. The length scale $\Delta$ is assumed to be equal to the average of the grid distances ($\Delta = 73.3$ m, for values in Table 1) rather than the root mean cube [$\Delta' = [\Delta x\Delta y\Delta z)^{1/3} = 58.2$ m], as assumed by Deardorff (1974). Deardorff's form was recently shown to be correct by Scotti et al. (1993). For grid anisotropy Scotti et al. (1993) proposed correction of constants in eddy diffusivity coefficients. For the aspect ratio $\Delta z/\Delta x = 1/5$ (Table 1), $c_s$ is recommended to be multiplied by 1.3. It can be noted however that, because the ratio of both length scales $\Delta$ and $\Delta'$ is also about 1.3, the recommended decrease of the length scale and the increase of $c_s$ cancel each other and, consequently, any correction is necessary.

### c. *Boundary conditions and numerical scheme*

Horizontal boundary conditions were assumed to be periodic. At the lower boundary, constant (in time and space) surface temperature and humidity fluxes were assumed, $H_0 = 0.001$ K m s$^{-1}$ and $Q_0 = 0.005$ g kg$^{-1}$ m s$^{-1}$. The vertical derivative of the turbulent kinetic energy was assumed to be zero. The Monin–Obukhov similarity formulation was employed to calculate momentum fluxes (e.g., Schmidt and Schumann 1989). The upper boundary conditions were assumed to be stress free for horizontal velocity components and zero for vertical velocity. Moreover, a specified lapse rate $\Gamma$ for temperature (0 K km$^{-1}$ or 3 K km$^{-1}$), zero lapse rate for humidity, and zero turbulent kinetic energy were assumed at the top of the domain.

The numerical algorithm of the model was developed by Deardorff (1973a,b). Adams–Bashforth's scheme was employed for integration in time. Adams–Bashforth's scheme is known to be unconditionally unstable; nevertheless, because the instability is weak and because of stabilizing effects of the viscous terms, the method can be successfully used in practice. Central finite differences were used to approximate space derivatives on Arakawa's staggered mesh C grid with uniform spacing. All scalar quantities were located in the center of a grid volume. The Poisson equation for pressure was obtained by imposing a zero finite-difference divergence operator upon the finite-difference analog of the momentum equations in (1). The obtained equation was solved by fast Fourier transform in the horizontal and three-diagonal algorithm in the vertical. A numerical "sponge" was applied in the upper portion of the model (the top 10 grid points) to reduce reflection of gravity waves (Nieuwstadt et al. 1992).

Initially, the atmosphere was assumed to be at rest. The initial potential temperature profile was constant (=300 K) with height within the mixed layer. Above the mixed layer the temperature increased with a constant positive lapse rate $\Gamma$. Initial random perturbations were imposed upon the temperature field within the mixed layer (e.g., Nieuwstadt et al. 1992). The initial potential humidity profile was constant (=1 g kg$^{-1}$) with height within the mixed layer and zero above. The geostrophic wind and the Coriolis terms were assumed to be zero. The roughness length was $z_0 = 0.16$ m.

### d. *Characteristics of performed simulations*

The parameters characterizing the simulations performed are presented in Table 1. In the table, N refers to the nonpenetrative simulation, and P to the penetrative simulation. Symbols $\Delta t$, $\Delta x$, $\Delta y$, and $\Delta z$ indicate time and space increments; $w_* = (\beta z_i H_0)^{1/3}$, $T_* = H_0/w_*$, and $q_* = Q_0/w_*$ are the convective scales for vertical velocity, temperature, and humidity, respectively; $z_i$ is the mixed-layer height (defined as the height where the temperature heat flux has the minimum value), $L$ is the Monin–Obukhov length, and $t_* = z_i/w_*$ is the convective timescale.

Runs N and P differ in the temperature lapse rate $\Gamma$ at the top of the computational domain. The temperature lapse rate $\Gamma$ was 3 K km$^{-1}$ for run P. In run N the upper boundary was insulated ($\Gamma = 0$) and moisture impermeable. In order to minimize effects of the upper boundary, the computational domain during run P extends to $2z_i = 1100$ m. The computational domain during run N is $z_i = 600$ m. The sponge coefficient in run P was 0.01 s$^{-1}$. The numerical sponge was turned off during the N simulation.

Krettenauer and Schumann (1992) used 64 × 64 × 16 grid points in their simulation of nonpenetrative convection. Their model was run for a time interval of $t = 35t_*$ and averaged the results within a period of $5t_*$. As can be seen in Table 1, run N uses 32 × 32 × 30 grid points, while there are 32 × 32 × 55 grid points in run P. Consequently, runs N and P use fewer grid points in the horizontal and a larger amount of grid points in the vertical with respect to Krettenauer and Schumann's (1992) simulation. It should be mentioned

TABLE 1. Characteristics of performed simulations.

| Run | Time steps | Space domain | $\Delta t$ (s) | $\Delta x = \Delta y$ (m) | $\Delta z$ (m) | $w_*$ (m s$^{-1}$) | $T_*$ (K) | $q_*$ (g kg$^{-1}$) | $z_i$ (m) | $-z_i/L$ | $t_*$ (s) |
|---|---|---|---|---|---|---|---|---|---|---|---|
| N | 6000 | 32 × 32 × 30 | 2.5 | 100 | 20 | 0.267 | 0.0037 | 0.019 | 600 | 120.0 | 37.5 |
| P | 6000 | 32 × 32 × 55 | 2.5 | 100 | 20 | 0.262 | 0.0038 | 0.019 | 550 | 161.2 | 35.0 |

that Schumann (1991b) and Nieuwstadt et al. (1992) have shown that basic characteristics of turbulence can be accurately represented even by a low number of grid points.

Calculations were performed in a horizontal domain size of $5.5z_i$ for run N and $5.8z_i$ for run P. A domain of size of $4z_i$ is considered by Krettenauer and Schumann (1992) to be sufficient and is also the minimum to cover all important scales. Sykes and Henn (1988) investigated the impact of increasing numerical resolution and increasing domain size. They found that differences between the runs with different domain sizes are small.

The time integration during run N was performed over a period of $6.7t_*$, with $t_* \approx 37.5$ min. The time integration during run P was performed over a period of $7.1t_*$, with $t_* \approx 35$ min. Figure 1 indicates that the kinetic energy in run N becomes approximately steady after about 5000 time steps, which is $5.6t_*$. A similar plot (not shown) was also obtained for run P. Figure 1 shows that the subgrid portion of the turbulent kinetic energy in simulation N (as well as in run P) amounts to about 30% of the total kinetic energy. Therefore, 70% of turbulent kinetic energy is directly resolved in this calculation. Consequently, the simulations performed can be classified as LESs. For comparison, in the simulation of Krettenauer and Schumann (1992) about 80% of turbulent kinetic energy was directly resolved.

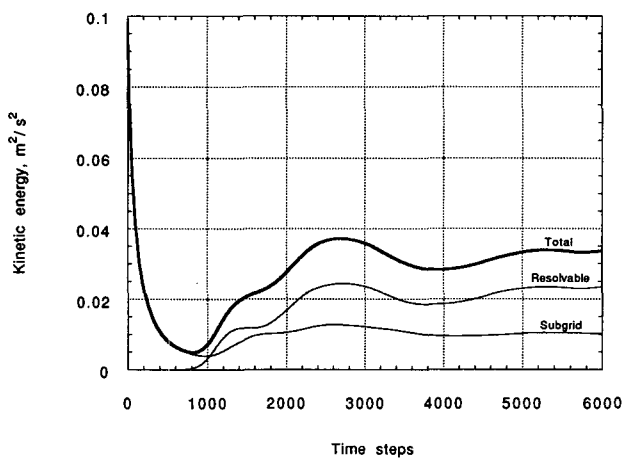


FIG. 1. Time history of the kinetic energy during run N.

The results of all simulations were averaged in time and also horizontally in space. The time averaging was executed during the last 500 time steps, every 50 time steps during run N and every 25 time steps during run P. Large values of the parameter $-z_i/L$ in Table 1 during both simulations indicate extremely convective conditions, even though $w_*$ and $z_i$ are relatively small.

## 3. The results

### a. General description of thermal convection

The vertical profiles of the total and subgrid virtual potential temperature fluxes are shown in Fig. 2. The total fluxes are defined as $H = \langle w'\theta' \rangle$ + sgc, where $\langle\ \rangle$ indicates an averaged quantity (over time and horizontally in space); the primed quantities are defined as departures from horizontal means. The subgrid component of the total flux is defined as sgc = $\langle H_3 \rangle$, where $H_3$ is described by (3). Figure 2 indicates that both total fluxes are linear within the mixed layer. As expected, the temperature flux at the top of the mixed layer vanishes in run N, while for run P the flux at the top of the mixed layer is negative and equal to about 25% of its surface value. The temperature flux in the penetrative case vanishes at $z = 1.2z_i$. The subgrid portion of the flux increases at the top of the penetrative mixed layer;

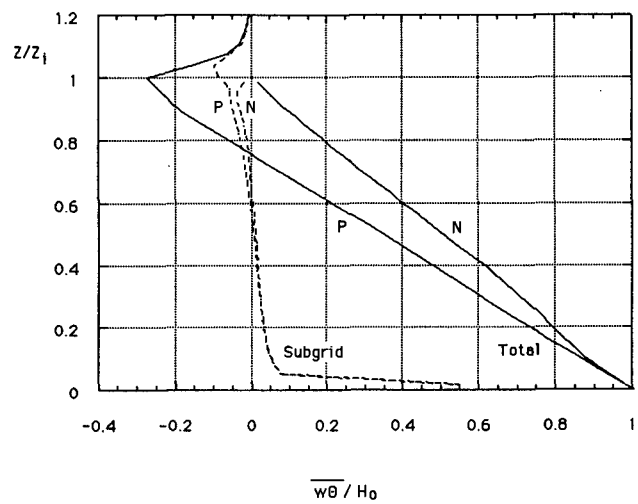


FIG. 2. Vertical distribution of the dimensionless total (solid line) and subgrid (dotted line) fluxes of the potential virtual temperature for runs N and P.

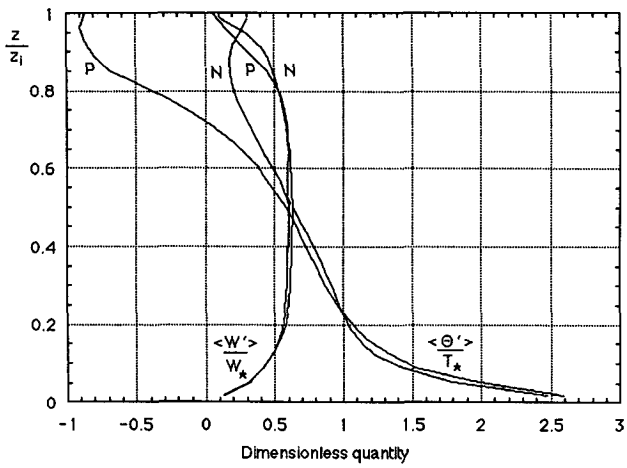


FIG. 3. Dimensionless mean excess of potential virtual temperature and vertical velocity in updrafts for runs N and P.

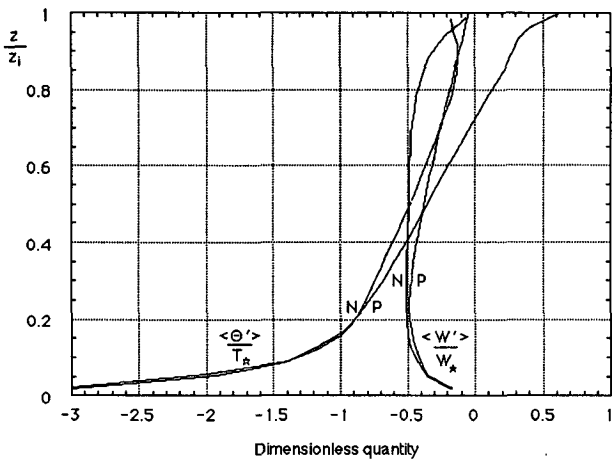


FIG. 4. Dimensionless mean excess of potential virtual temperature and vertical velocity in downdrafts for runs N and P.

nevertheless, it remains much smaller than the total flux.

Figure 3 shows the conditionally averaged dimensionless potential temperature excess (i.e., $\langle\theta'\rangle = \langle\theta\uparrow\uparrow - \{\theta\}\rangle$, $\theta\uparrow\uparrow$ is the temperature in updrafts, and $\{\ \}$ denotes horizontal averaging) and vertical velocity (i.e., $\langle w'\rangle = \langle w\uparrow\uparrow\rangle$, since $\{w\} = 0$) in updrafts during runs N and P. Updrafts were identified by positive vertical velocities, $w\uparrow\uparrow > 0$. It is interesting to see that the dimensionless vertical velocity in updrafts during the penetrative convection is nearly the same as in the nonpenetrative case. The temperature excesses in updrafts in runs N and P coincide up to approximately $0.5z_i$. Above this level updrafts in run P are relatively cooler, due to heating of the upper portion of the mixed layer by entraining warm air from the capping stable layer.

The dimensionless mean temperature excess and vertical velocity in downdrafts (identified by negative vertical velocities) in both simulations are presented in Fig. 4. Temperature excesses in downdrafts in runs P and N coincide only below $0.2z_i$. Above, downdrafts in run P are relatively warmer as they carry entrained warm air from the capping stable layer. The vertical velocities in downdrafts during both simulations are the same up to approximately $0.4z_i$. Above this level the vertical velocity of downdrafts during run P is slightly smaller. This is caused by the fact that downdrafts in run P are positively buoyant. In contrast, in the nonpenetrative case downdrafts are negatively buoyant and sink relatively faster. The shape of the vertical velocity profiles and temperature profiles in updrafts and downdrafts is nearly symmetric. The magnitude of vertical velocity in updrafts is slightly larger than in downdrafts, which agrees with atmospheric observations of Young (1988).

The temperature flux vanishes at the top of the nonpenetrative domain due to vanishing of the vertical velocity at the boundary. During penetrative convection, the vertical velocity in updrafts at the top of the mixed layer is small but positive, and the temperature excess is relatively large and negative (Fig. 3). Consequently, on average updrafts at the top of the penetrative mixed layer contribute to the negative temperature flux. On the other hand, the vertical velocity in downdrafts near the top of the mixed layer is small and negative, while the temperature excess is relatively large and positive (Fig. 4). Thus, downdrafts at the top of the penetrative mixed layer also contribute on average to the negative temperature flux. The resulting total temperature flux is negative near the top of the mixed layer during penetrative convection. A similar conclusion was obtained by Schumann and Moeng (1991).

Figure 5 shows that in the bulk of the mixed layer the relative area covered by updrafts during run N is approximately constant with height. This agrees with

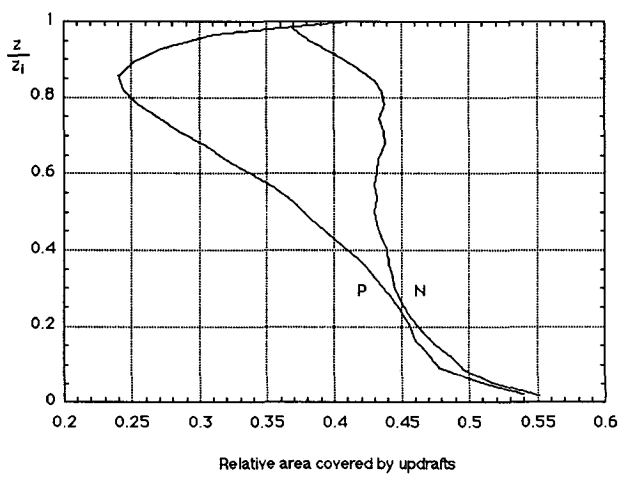


FIG. 5. Relative area covered by updrafts during runs N and P.

the result of Moeng and Rotunno (1990). The figure indicates that updrafts cover $A\Uparrow = 43\%$, while the relative area covered by downdrafts is $A\Downarrow = 57\%$. It can be noticed that since the horizontally averaged vertical velocity must vanish (mass continuity restraint), then

$$A\Uparrow \langle w\Uparrow \rangle + A\Downarrow \langle w\Downarrow \rangle = 0. \quad (9)$$

Substituting values of $A\Uparrow$ and $A\Downarrow$ yields $\langle w\Uparrow \rangle = -1.3\langle w\Downarrow \rangle$. For $\langle w\Downarrow \rangle = -0.5w_*$ (see Fig. 4), we obtain that $\langle w\Uparrow \rangle = 0.65w_*$, which agrees with Fig. 3. Consequently, nonpenetrative convection is composed of narrower updrafts with larger velocities and wider and slower downdrafts. A similar process is also observed in penetrative convection.

The relative area covered by updrafts in run P has a minimum near the top of the mixed layer. A similar conclusion was obtained by Moeng and Rotunno (1990) based on Moeng's LES model (1984). The minimum value of $A\Uparrow$ produced by Moeng's model is about 40% (e.g., Schumann and Moeng 1991). It can be noticed in Fig. 5 that $A\Uparrow$ is about 25% in run P. A comparison of various LES codes performed by Nieuwstadt et al. (1990) confirms that Schumann's subgrid parameterization, described in section 2a, yields relatively small values of $A\Uparrow$.

In Fig. 6, the vertical cross sections of an instantaneous vertical velocity field are depicted for nonpenetrative convection. The figure shows that nonpenetrative convection is organized into separate columns of updrafts and downdrafts extending from the bottom to the top of the domain. A similar result was also obtained by Moeng and Rotunno (1990). Moeng and Rotunno observed that updrafts line up as irregular polygons in the lower levels and are more isolated above. Updrafts that originate at the intersections of these polygons are more likely to survive to the upper levels.

During penetrative convection, the area covered by updrafts decreases with height. According to Schmidt and Schumann (1989), large thermals have higher thermal velocity and suck in smaller thermals from their neighborhood. Since updrafts in penetrative convection are negatively buoyant and downdrafts are positively buoyant, work has to be performed against buoyancy to support vertical motions of air near the top of the mixed layer and above it. The magnitude of the work performed, $W$ (for a unit of mass over a unit of time), is proportional to the negative area in Fig. 2. The negative area is located between the curve representing the flux and the $z$-axis, from the level $h_0$ at which the heat flux crosses zero to the level $h \approx 1.2z_i$ where the heat flux vanishes. The buoyant production of turbulent kinetic energy (for a unit of mass over a unit of time) is proportional to the positive area in the same figure, from the surface to the level $h_0$. Both quantities $W$ and $P$ can be estimated as follows:

$$W = \int_{h_0}^{h} \beta H dz = 0.5 \frac{w_*^3}{1-R}(1.2R^2 - 0.2R)$$

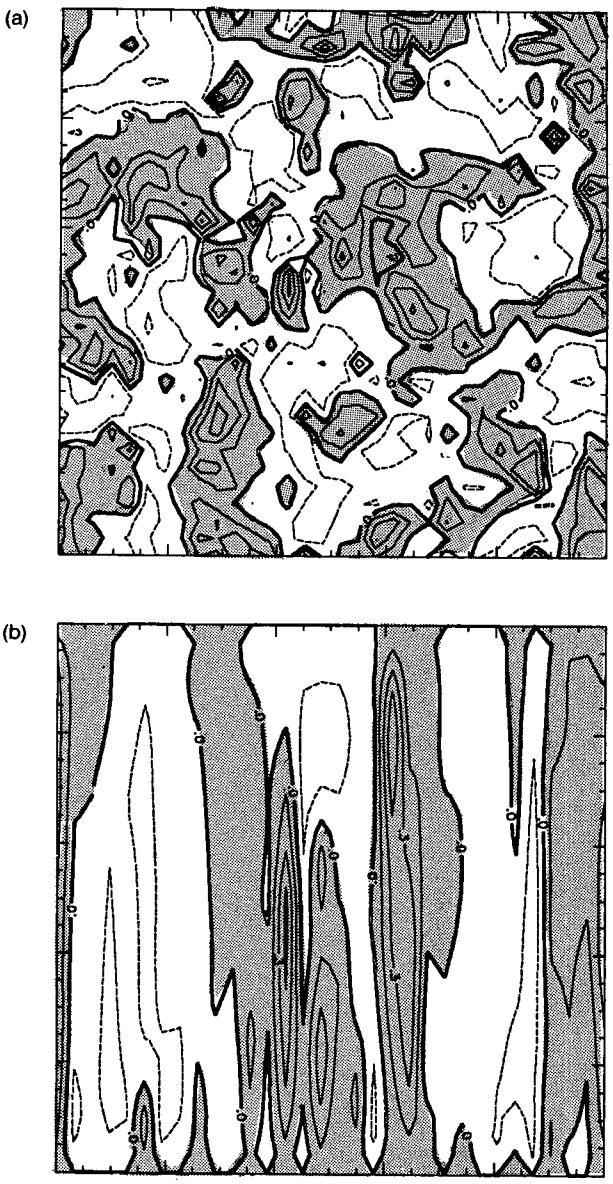


FIG. 6. (a) Horizontal ($x$–$y$) and (b) vertical ($x$–$z$) cross sections of an instantaneous vertical velocity field during nonpenetrative convection. The horizontal cross section is obtained at $z = 0.5z_i$; the vertical cross section is obtained at $y = 0.5L$. Contour interval $= 0.15w^*$. Regions with positive velocities are shaded.

$$P = \int_0^{h_0} \beta H dz = 0.5 \frac{w_*^3}{1-R}, \quad (10)$$

where $R$ is the heat flux ratio $R = H_i/H_0$ and $h_0 = z_i/(1 - R)$ is the height at which the heat flux crosses zero (Sorbjan 1995). In (10) the temperature flux was assumed to be linear and equal to $H = H_0(1 - z/z_i)$ for nonpenetrative convection. In the case of penetrative convection two linear profiles were used: $H = H_0[(1 - z/z_i) + Rz/z_i]$ for $z \leq z_i$ and $H = 5RH_0(1.2 - z/z_i)$ for $z_i < z \leq 1.2z_i$.

If we compare areas of positive and negative regions of the heat flux, it can be seen that $W = (1.2R^2 - 0.2R)P$. This suggests that for $R = -0.2$ about $(1.2R^2 - 0.2R) \approx 9\%$ of the turbulent kinetic energy generated by surface heating goes to support entrainment. Some other previously presented estimates range from 4% to 20% and were discussed by Lilly (1989).

Analysis of Figs. 2–6 brings the following picture of the nonpenetrative convection. Rising fluid is initially accelerated by buoyancy. The acceleration decreases with height because thermals lose their buoyancy through a heat transfer to the surrounding fluid. Deceleration occurs when updrafts approach the upper boundary. At the top a rigid lid forces the fluid to spread. After this horizontal spreading, the temperature of air that was formerly in the thermals becomes lower than the mean temperature of the mixed layer (which is steadily warming). Consequently, the ascending thermals are converted into a cool, descending flow. The full cycle, consisting of a rising and a sinking phase, lasts approximately $z_i/(0.5w_*) + z_i/(0.65w_*) = 3.5t_*$, where the vertical velocities were estimated based on Figs. 3 and 4.

In the case of penetrative convection rising fluid is also initially accelerated by buoyancy. The acceleration decreases with height. Deceleration occurs when updrafts encounter a descending positively buoyant flow or enter the entrainment zone. Updrafts, which are on average negatively buoyant, are still able to penetrate the stable layer. The penetration forces entrainment of warm air into the mixed layer. Downdrafts are on average positively buoyant. They gradually lose their buoyancy through a heat transfer to the surrounding fluid.

In Fig. 7, the dimensionless components of the resolvable turbulent kinetic energy budget are depicted for both runs, N and P. In the figure, DD = $\langle\epsilon\rangle$ is the averaged dissipation term calculated based on (7), BP = $\beta\langle w'\theta'\rangle$ is the buoyant production term, TT = $0.5\, d/dz\langle u'^2w' + v'^2w' + w'^3\rangle$ is the turbulent transport term, PP = $d/dz\langle w'P'\rangle$ is the pressure transport term, and SP = $-(\langle u'w'\rangle d\langle\bar{u}\rangle/dz + \langle v'w'\rangle d\langle\bar{v}\rangle/dz)$ is the shear production. Generally, the turbulent kinetic energy is generated by buoyancy BP and lost due to the viscous dissipation DD. The turbulent transport redistributes energy from near the lower surface (negative values of TT) to the top (positive values of TT). The pressure transport term PP has a tendency to oppose this transfer. The strongest differences between penetrative and nonpenetrative cases are reflected upon the largest components of the energy balance, that is, in dissipation DD and in buoyancy production BP.

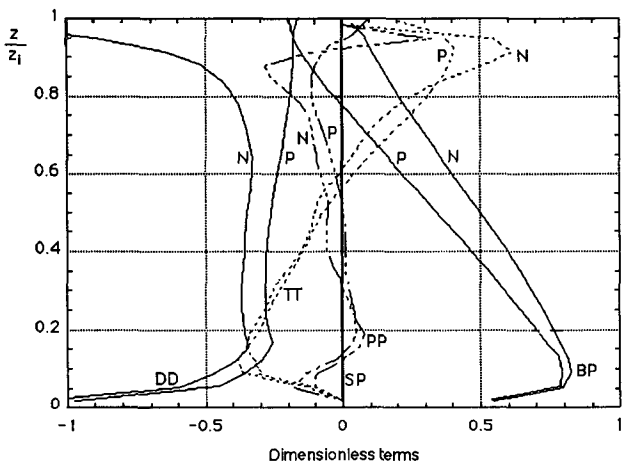


FIG. 7. Dimensionless components of the resolvable kinetic turbulent energy balance during runs N and P. All terms scaled by $w_*^3/z_i$.

For steady-state, nonpenetrative convection the mixed-layer averaged value of the dissipation $\epsilon_N$ should be exactly equal to the mean buoyancy production; that is,

$$\epsilon_N = \frac{1}{z_i}\int_0^{z_i} H_0(1 - z/z_i)dz = 0.5w_*^3/z_i. \quad (11)$$

Similarly, for a steady state of penetrative convection,

$$\epsilon_P = 0.5\,\frac{(1 + R)w_*^3}{(1 - R)z_i}. \quad (12)$$

Consequently,

$$\epsilon_P/\epsilon_N = (1 + R)/(1 - R). \quad (13)$$

This suggests that dissipation in penetrative convection equals about $(1 + R)/(1 - R) = 67\%$ of the dissipation generated in the nonpenetrative case (for $R = -0.2$). This agrees with values in Fig. 7.

### b. *Temperature fields*

Dimensionless profiles of the potential temperature lapse rate during runs N and P are shown in Fig. 8. Both profiles coincide up to the level $z/z_i = 0.5$. Above $z/z_i = 0.6$, the profile for run N is positive, which indicates the countergradient transport of heat in this region. The countergradient transport of heat for run P takes place in a layer $0.5 < z/z_i < 0.75$, where both the lapse rate and the flux are positive.

Figure 9 shows profiles of the dimensionless total and subgrid temperature variance during runs N and P. The total temperature variance is defined as $\sigma_\theta^2 = \langle\theta'^2\rangle + \text{sgc}$, where the subgrid component of the total variance is defined as $\text{sgc} = 5\langle H_3\rangle^2/\langle E\rangle$, $\langle H_3\rangle$ is the averaged subgrid vertical temperature flux, and $\langle E\rangle$ is the averaged subgrid turbulent kinetic energy (Nieuwstadt et al. 1992).

Both total variances in Fig. 9 are in agreement up to the level $z/z_i = 0.8$. Near the top of the mixed layer the dimensionless variance for penetrative convection exhibits a rapid increase of its values. This fact can be explained by using an approximate expression, which

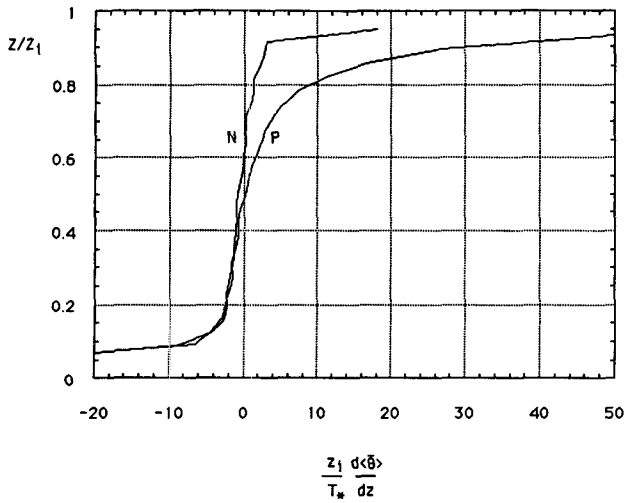


FIG. 8. Dimensionless lapse rate of potential virtual temperature for runs N and P.

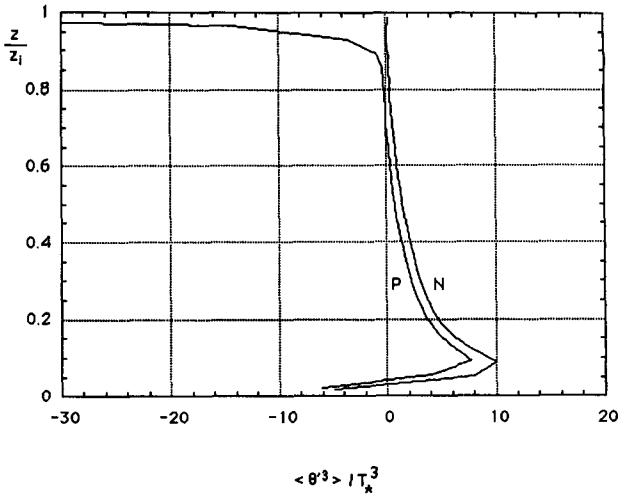


FIG. 10. Dimensionless third moment of the potential virtual temperature (resolvable) during runs N and P.

can be obtained from the simplified temperature variance equation, with only production and dissipation terms retained (Sorbjan 1989):

$$\frac{\langle\theta'^2\rangle}{\tau} \approx -\langle w'\theta'\rangle \frac{\partial\langle\bar{\Theta}\rangle}{\partial z}, \qquad (14)$$

where $\tau$ is the timescale. Since the temperature flux is negative at the top of the mixed layer, the above equation indicates that the temperature variance will increase if the temperature lapse rate increases.

A dimensionless third moment of temperature during runs N and P is shown in Fig. 10. The penetrative curve agrees with results obtained in a tank by Kumar et al. (1986). Both curves approximately coincide up to $z/z_i = 0.9$. Only the resolvable portion of the moment is shown in Fig. 10. Consequently, the values of the moment near the surface are not reliable.

### c. *Humidity fields*

Figure 11 depicts the dimensionless total specific humidity fluxes during runs N and P. The total fluxes are defined as $Q = \langle w'q'\rangle$ + sgc, where sgc denotes the subgrid component of the total flux defined as sgc $= \langle Q_3\rangle$. The total flux in run N is not exactly linear. This indicates that the simulation time in this run was too short to achieve steady state. The magnitude of the humidity flux at the top of the mixed layer is about 20% of the surface value in run P.

Dimensionless humidity lapse rates during runs N and P are shown in Fig. 12. In the figure, both profiles

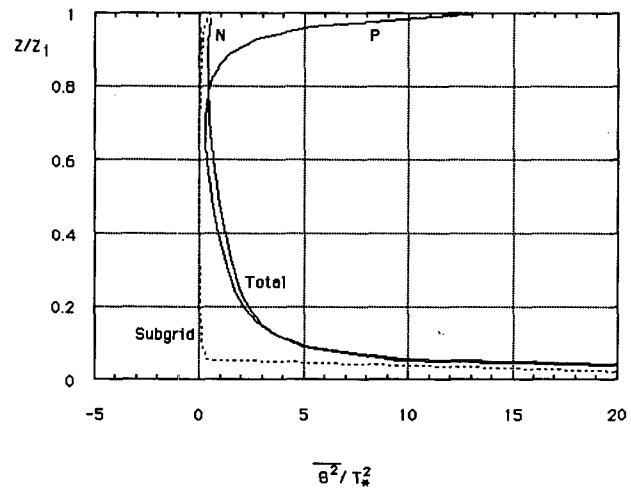


FIG. 9. Dimensionless total (solid line) and subgrid (dotted line) variances of potential virtual temperature for runs N and P.

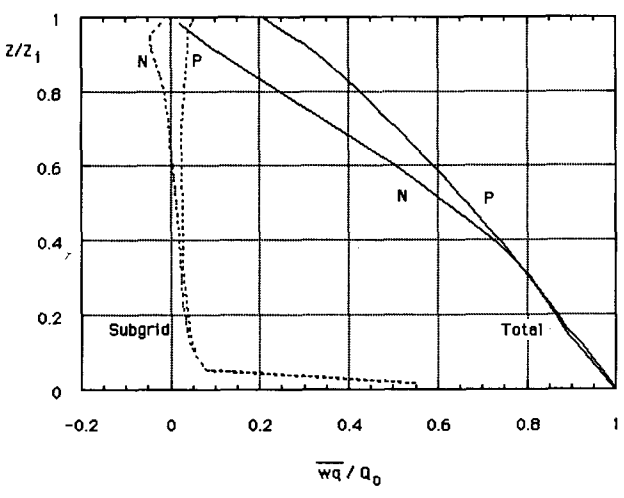


FIG. 11. Dimensionless total (solid line) and subgrid (dotted line) fluxes of specific humidity for runs N and P.

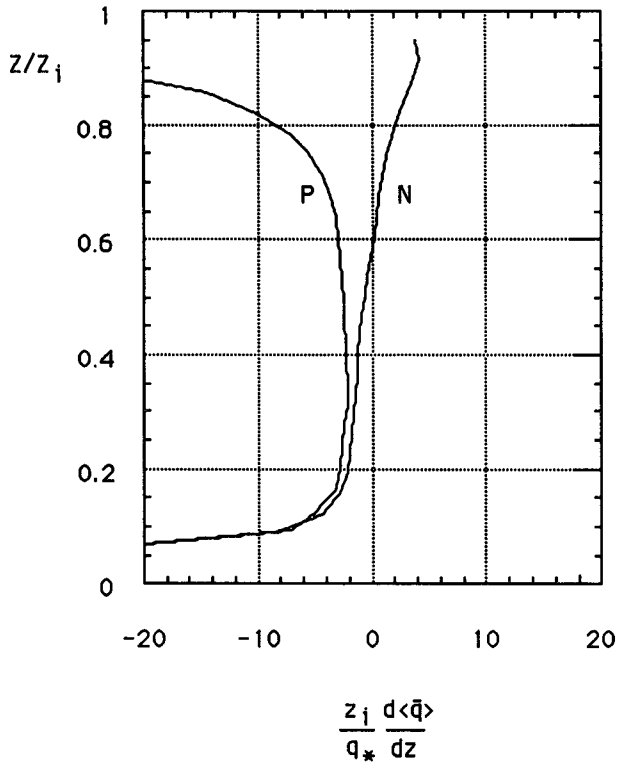


FIG. 12. Dimensionless lapse rate of specific humidity for runs N and P.

approximately coincide up to the level $z/z_i = 0.4$. Above $z/z_i = 0.6$, the nonpenetrative lapse rate is positive, which indicates the countergradient transport of moisture in the upper portion of the mixed layer. In the penetrative case the humidity flux in Fig. 11 is positive, while the humidity lapse rate in Fig. 12 is negative. Interestingly, this implies that the countergradient transport of humidity is not present in the penetrative case. A positive humidity lapse rate near the top of the nonpenetrative boundary layer denotes an accumulation of mass near the upper surface. The humidity lapse rate at the top in the penetrative case is negative and indicates drying by entrained air.

Wyngaard (1984) and Moeng and Wyngaard (1984) decomposed scalar fields C into "bottom up" and "top down" components, $C_b$ and $C_t$. The bottom-up component was assumed to be driven by the surface flux, while the top-down component was due to entrainment. For mean humidity fields, two similarity functions $g_b$ and $g_t$ were defined as

$$\frac{z_i \partial C_b}{c_* \partial z} = -g_b(z/z_i)$$

$$\frac{z_i \partial C_t}{c_* \partial z} = -R_c g_t(z/z_i), \qquad (15)$$

where $R_c$ is the scalar flux ratio at the top and the bottom of the mixed layer and $c_*$ is the convective scale defined analogously to $T_*$ and $q_*$.

In the nonpenetrative case we have $R = R_c = 0$. Consequently, the bottom-up function $q_b$ is identical to the dimensionless humidity lapse rate in our nonpenetrative run shown in Fig. 12. The difference of the dimensionless lapse rates in penetrative and nonpenetrative cases in Fig. 12 defines the top-down function $g_t$. A similar approach was adopted by Sorbjan (1989), who proposed to decompose dimensionless statistics of turbulence during penetrative convection into nonpenetrative and residual components. Consequently, his decomposition and Wyngaard's (1984) bottom-up and top-down decomposition are equivalent in the considered case.

Moeng and Wyngaard (1984) assumed that the bottom-up and top-down decomposition applies to humidity and temperature fields alike. Validity of this assumption can be verified by comparing Figs. 8 and 12. The comparison shows that the dimensionless temperature and humidity lapse rates for nonpenetrative convection are equal:

$$\frac{z_i \partial q}{q_* \partial z} = \frac{z_i \partial \Theta}{T_* \partial z}. \qquad (16)$$

Dimensionless total humidity variances during runs N and P are shown in Fig. 13. The total humidity variance is defined as $\sigma_q^2 = \langle q'^2 \rangle + \text{sgc}$, where the subgrid component of the total variance is defined as $\text{sgc} = 5\langle Q_3 \rangle^2 / \langle E \rangle$, $\langle Q_3 \rangle$ is the averaged subgrid vertical humidity flux, and $\langle E \rangle$ is the averaged subgrid turbulent kinetic energy.

Inspection of Figs. 9 and 13 indicates that dimensionless total variances for temperature and humidity are approximately equal in the nonpenetrative case.

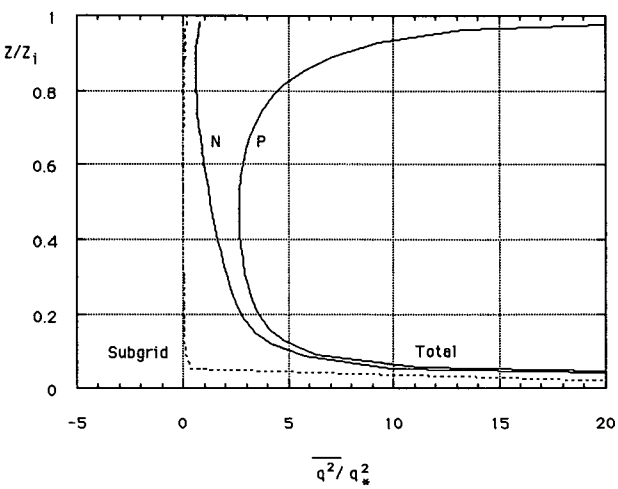


FIG. 13. Dimensionless total (solid line) and subgrid (dotted line) variances of specific humidity for runs N and P.

This fact can also be confirmed in Fig. 14, which shows that temperature and humidity during nonpenetrative convection are perfectly correlated (with numerical accuracy). This is a consequence of the fact that both scalars follow the same governing equations and have analogous boundary conditions. During penetrative convection, $r_{\theta q}$ is less than unity and varies from about 0.9 near the surface to about $-0.7$ at the top of the mixed layer.

The correlation coefficient $r_{\theta q}$ in the surface layer was reported to be less than unity by many investigators. For instance, Wyngaard et al. (1978), after analysis of data collected in convective conditions over the East China Sea, concluded that $r_{\theta q} \approx 0.8$. During convective conditions over land, Druilhet et al. (1983) obtained $r_{\theta q} \approx 0.6$. Guillement and Isaka (1983), from a series of measurements in convective conditions over land, evaluated that $r_{\theta q} = 0.54$ in the inertial subrange. Sorbjan (1991) found that in convective conditions $r_{\theta q} = 0.76$. Deardorff (1974), in his large eddy simulation of the Wangara data, obtained the correlation coefficient $r_{\theta q}$ (between resolvable quantities) to be about 0.6 near the surface. Our results imply that the lack of perfect correlation during penetrative convection is caused by the drying effects of entrainment.

### d. *Velocity fields*

Dimensionless total horizontal and vertical velocity variances $\sigma_u^2$, $\sigma_v^2$ and $\sigma_w^2$ during runs N and P are shown in Fig. 15. Each of the total velocity variances consists of resolvable and subgrid terms. For instance, $\sigma_u^2 = \langle u'^2 \rangle$ + sgc, where the subgrid component sgc $= \frac{2}{3}\langle E \rangle$, and $\langle E \rangle$ is the averaged subgrid turbulent kinetic energy. The curves obtained in run N are in accord with results of Krettenauer and Schumann (1992), while the curves simulated in run P coincide with results presented by Nieuwstadt et al. (1992).

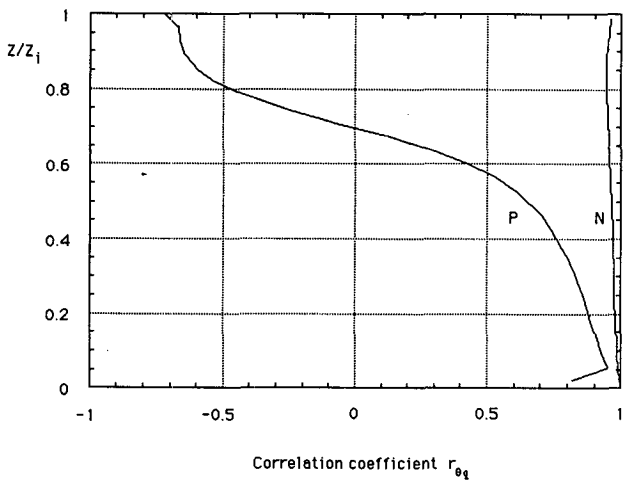


FIG. 14. Correlation coefficient between potential virtual temperature and specific humidity for runs N and P.

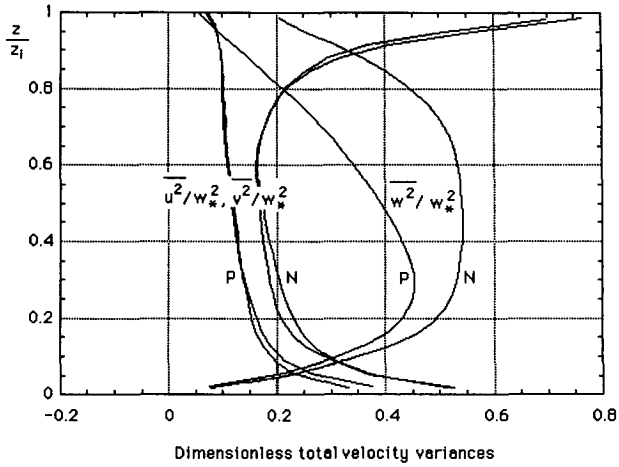


FIG. 15. Dimensionless total variances of horizontal and vertical components of velocity during runs N and P. All terms scaled by $w_*^2$.

Values of the dimensionless variances in the nonpenetrative case are larger than in the penetrative one. This fact is related to the reduction of the dissipation rate described by (13). Assuming in this equation that the dissipation is related to the total turbulent kinetic energy $E_t = \langle u_k'^2 \rangle/2 + \langle E \rangle$ as $\epsilon \sim E_t^{3/2}/z_i$, we obtain the ratio for both runs, $E_t^P/E_t^N = [(1 + R)/(1 - R)]^{2/3}$. For $R = -0.2$, we estimate that $E_t^P/E_t^N \sim 0.76$. Consequently, the total turbulent kinetic energy during penetrative convection is reduced by about 24% with respect to the nonpenetrative case. The reduction is due to mixing of the entrained air with the mixed-layer air. Assuming the same reduction for each of the velocity variances, we obtain that velocity variances should be reduced by about $\frac{2}{3}(24\%) = 16\%$. It can be examined by inspection that this estimate agrees with Fig. 15.

Near the top of the mixed layer in Fig. 15 values of the dimensionless horizontal variances in nonpenetrative case are larger than near the lower surface. This effect can be related to the fact that lower boundary conditions assume the presence of a drag while the boundary condition at the top of the domain is stress free. Effects of "no slip" and "free slip" boundary conditions in nonpenetrative convection were considered by Moeng and Rotunno (1990).

## 4. Concluding remarks

A large eddy simulation model was used to compare statistics of turbulence during nonpenetrative and penetrative dry convection. The comparison showed that the presence of entrainment significantly alters the dynamics of the mixed layer. In the nonpenetrative case convection is organized into separate columns of updrafts and downdrafts extending from the bottom to the top of the domain. In penetrative convection updrafts

are embedded in slowly sinking air, and their horizontal area decreases with height.

In penetrative convection dimensionless vertical velocity in updrafts is almost the same as in the nonpenetrative case. In the upper half of the mixed layer updrafts in the penetrative case are relatively cooler than the ambient air, due to heating of the upper portion of the mixed layer by entraining warm air from the capping stable layer. Downdrafts are initially warmer as they carry the entrained warm air.

The countergradient transport of heat and moisture during nonpenetrative convection takes place for $z/z_i > 0.6$. For run P the countergradient transport of heat occurs in a layer $0.5 < z/z_i < 0.75$, while the countergradient transport of humidity is not present.

During nonpenetrative convection, temperature and humidity are perfectly correlated. During penetrative convection, the correlation coefficient is less than unity and varies from about 0.9 near the surface to about $-0.7$ at the top of the mixed layer. This decorrelation is due to entrainment.

About 9% of the turbulent kinetic energy generated by surface heating goes to support entrainment. Entrainment reduces the dissipation rate to about 70% of the dissipation generated in the nonpenetrative case. The turbulent kinetic energy during the penetrative convection is reduced by about 24% with respect to the nonpenetrative case. Velocity variances are reduced by about 16%.

*Acknowledgments.* This research was sponsored by NSF Grant ATM 9217028. The author would like to thank Dr. Douglas Lilly, Dr. Chin-Hoh Moeng, Dr. N. Andrew Crook, and Dr. Richard Doviak for their valuable comments.

## REFERENCES

Adrian, R. J., R. T. D. S. Ferreira, and T. Boberg, 1986: Turbulent thermal convection in wide horizontal fluid layers. *Expts. in Fluids,* **4,** 121–141.

Agee, E. M., 1987: Mesoscale cellular convection over oceans. *Dyn. Atmos. Oceans,* **10,** 317–341.

Boers, R., 1989: A parameterization of the depth of the entrainment zone. *J. Appl. Meteor.,* **28,** 107–111.

Caughey, S. J., and S. G. Palmer, 1979: Some aspects of turbulence structure through the depth of the convective boundary layer. *Quart. J. Roy. Meteor. Soc.,* **105,** 811–827.

Coleman, G. N., J. H. Ferziger, and P. R. Spalart, 1990: A numerical study of the turbulent Ekman layer. *J. Fluid Mech.,* **213,** 313–348.

Deardorff, J. W., 1972: Numerical integration of neutral and unstable planetary boundary layers. *J. Atmos. Sci.,* **29,** 91–115.

——, 1973a: Three-dimensional numerical modelling of the planetary boundary layers. *Workshop on Micrometeorology,* D. A. Haugen, Ed., Amer. Meteor. Soc., 271–311.

——, 1973b: The use of subgrid transport equations in a three-dimensional model of atmospheric turbulence. *J. Fluids Eng.,* **95,** 429–438.

——, 1974: Three-dimensional numerical study of turbulence in an entraining mixed layer. *Bound.-Layer Meteor.,* **7,** 199–226.

——, G. E. Willis, and D. K. Lilly, 1969: Laboratory investigation of non-steady penetrative convection. *J. Fluid Mech.,* **35,** 7–31.

——, ——, and B. H. Stockton, 1980: Laboratory studies of entrainment zone of a convectively mixed layer. *J. Fluid Mech.,* **100,** 41–64.

Druilhet, A., J. P. Frangi, D. Guadalia, and J. Fontan, 1983: Experimental studies of the turbulence structure parameters of the convective boundary layer. *J. Climate Appl. Meteor.,* **22,** 594–608.

Guillemet, B., and H. Isaka, 1983: Molecular dissipation of turbulent fluctuations in the convective mixed layer. Part I: Height variations of dissipation rates. *Bound.-Layer Meteor.,* **27,** 141–162.

Krettenauer, K., and U. Schumann, 1992: Numerical simulation of turbulent convection over wavy terrain. *J. Fluid Mech.,* **237,** 261–299.

Kumar, R., and R. J. Adrian, 1986: Higher order moments in the entrainment zone of turbulent penetrative thermal convection. *J. Heat Trans.,* **108,** 323–329.

Lilly, D. K., 1968: Models of cloud-capped mixed layers under a strong inversion. *Quart. J. Roy. Meteor. Soc.,* **94,** 292–309.

——, 1987: Modes of turbulence in stably stratified environments: Part II. *Lecture Notes on Turbulence,* J. R. Herring and J. C. McWilliams, Eds., World Scientific, 171–217.

——, 1995: A comparison of incompressible, anelastic, and Boussinesq dynamics. *Atmos. Res.,* submitted.

——, D. E. Waco, and S. I. Adelfang, 1974: Stratosphere mixing estimated from high-altitude turbulence measurements. *J. Appl. Meteor.,* **13,** 488–493.

Mahrt, L., 1979: Penetrative convection at the top of a growing boundary layer. *Quart. J. Roy. Meteor. Soc.,* **105,** 969–985.

Mason, P. J., 1989: Large-eddy simulation of the convective atmospheric boundary layer. *J. Atmos. Sci.,* **46,** 1492–1516.

——, 1994: Large-eddy simulation: A critical review of the technique. *Quart. J. Roy. Meteor. Soc.,* **120,** 1–26.

Moeng, C.-H., 1984: A large-eddy-simulation model for the study of planetary boundary-layer turbulence. *J. Atmos. Sci.,* **41,** 2052–3169.

——, and J. C. Wyngaard, 1984: Statistics of conservative scalars in the convective boundary layer. *J. Atmos. Sci.,* **41,** 3161–2062.

——, and R. Rotunno, 1990: Vertical velocity skewness in the buoyancy-driven boundary layer. *J. Atmos. Sci.,* **47,** 1149–1162.

Nieuwstadt, F. T. M., 1990: Direct and large-eddy simulation of free convection. *Proc. Ninth Int. Heat Transfer Conf.,* Vol. 1, Jerusalem, Israel, American Society Mechanical Engineers, 37–47.

——, and R. A. Brost, 1986: Decay of convective turbulence. *J. Atmos. Sci.,* **43,** 532–546.

——, P. J. Mason, C. H. Moeng, and U. Schumann, 1992: Large-eddy simulation of convective boundary-layer: A comparison of four computer codes. *Turbulent Shear Flows 8,* H. Durst et al., Eds., Springer-Verlag, 343–367.

Schemm, C. E., and F. B. Lipps, 1976: Some results from a simplified three-dimensional numerical model of atmospheric turbulence. *J. Atmos. Sci.,* **33,** 1021–1041.

Schmidt, H., and U. Schumann, 1989: Coherent structure of the convective boundary layer derived from large-eddy simulation. *J. Fluid Mech.,* **200,** 511–562.

Schumann, U., 1991a: Subgrid length-scales for large-eddy simulation of stratified turbulence. *Theor. Comput. Fluid Dyn.,* **2,** 279–290.

——, 1991b: Simulations and parameterizations of large eddies in convective atmospheric boundary layers. *Workshop on Fine Scale Modelling and the Development of Parameterization Schemes,* European Centre for Medium-Range Weather Forecasts, 21–51.

——, and C.-H. Moeng, 1991: Plume fluxes in clear and cloudy convective boundary layers. *J. Atmos. Sci.,* **48,** 1746–1757.

Scotti, A., C. Meneveau, and D. K. Lilly, 1993: Generalized Smagorinsky model for anisotropic grids. *Phys. Fluids A,* **5**(9), 2306–2308.

Sommeria, G., 1976: Three-dimensional simulation of turbulent processes in an undisturbed trade wind boundary layer. *J. Atmos. Sci.,* **33,** 216–241.

Sorbjan, Z., 1989: *Structure of the Atmospheric Boundary Layer.* Prentice-Hall, 317 pp.

——, 1991: Evaluation of local similarity functions in the convective boundary layer. *J. Appl. Meteor.*, **30,** 1565–1583.

——, 1995: Toward evaluation of heat fluxes in the convective boundary layer. *J. Appl. Meteor.*, **34,** 1092–1098.

Sullivan, P. P., J. C. McWilliams, and C.-H. Moeng, 1994: A subgrid-scale model for large-eddy simulations of planetary boundary-layer flows. *Bound.-Layer Meteor.*, **71,** 247–276.

Sykes, R. I., and D. S. Henn, 1988: A large-eddy simulation of turbulent sheared convection. *J. Atmos. Sci.*, **46,** 1106–1118.

Young, G. S., 1988: Turbulence structure of the convective boundary layer. Part II: Phoenix 78 aircraft observations of thermals and their environment. *J. Atmos. Sci.*, **45,** 727–735.

Weinstock, J., 1978: Vertical diffusion in a stably stratified fluid. *J. Atmos. Sci.*, **35,** 1022–1027.

Willis, G. E., and J. W. Deardorff, 1974: A laboratory model of the unstable planetary boundary layer. *J. Atmos. Sci.*, **31,** 1297–1307.

Wyngaard, J. C., 1984: Toward convective boundary layer parameterization: A scalar transport module. *J. Atmos. Sci.*, **41,** 102–112.

——, 1992: Atmospheric turbulence. *Annu. Rev. Fluid Mech.*, **24,** 205–235.

——, W. T. Pennell, D. H. Lenschow, and M. A. LeMone, 1978: The temperature-humidity covariance budget in the convective boundary layer. *J. Atmos. Sci.*, **35,** 47–58.

Zeman, D., and H. Tennekes, 1977: Parameterization of the turbulent energy budget at the top of the daytime atmospheric boundary layer. *J. Atmos. Sci.*, **34,** 111–123.